

Article

Dynamic behavior of a single bubble in cavity flow driven by a turbulent channel

Yuyun Bao [1], Xinyu Li [1], Ziqi Cai [1,*], Zhengming Gao [1,*], J.J. Derksen [2]

[1] State Key Laboratory of Chemical Resource Engineering, School of Chemical Engineering, Beijing University of Chemical Technology, Beijing 100029, China

[2] School of Engineering University of Aberdeen, Aberdeen AB24 3UE, UK

* Corresponding authors. Tel.: +8610 64418267; fax: +8610 64449862.

E-mail addresses: caiziqi@buct.edu.cn (Z. Cai), gaozm@buct.edu.cn (Z. Gao).

Abstract

Gas–liquid two-phase flow is a common phenomenon in both nature and industry processes. Predicting the behavioral trajectory of bubbles in complex flow fields is an aspect of gas–liquid flow, for which the analysis and understanding of the forces acting on the bubbles are necessary. This study investigates the motion of single bubbles about 2 mm in the recirculating flow in a quasi-two-dimensional cavity. The measured bubble trajectories and residence times we use to design a force-balance model of the bubble behavior. In the model we track the bubble through a single-phase flow field, including the turbulent fluctuations and their time scales. Key items of the model are the drag force and lift force on the bubble. We introduce the effective lift coefficient, which represents the combined effects of bubble deformation, turbulence and wall shear. By tuning the drag and – more importantly – the lift coefficient we achieve agreement between experimental and modeled bubble behaviors. Therefore, we are able to quantify the relative importance of the forces acting on the bubble, and offers an empirical framework for modeling deformable bubble dynamics in multiphase systems.

Keywords

Bubble dynamics; Bubble imaging; Force analysis; Particle image velocimetry

Highlights

The erratic bubble motion in a turbulent cavity has been visualized

The cavity flow has been accurately mapped by particle image velocimetry

Bubble trajectories have been calculated based on the PIV data and force correlations

To replicate experiments, an effective lift force coefficient has been developed

1. Introduction

Gas–liquid two-phase flow is common in industrial processes, especially in the devices such as bubble columns, stirred tanks, and gas–liquid separators. A thorough understanding of the bubble size distribution and dynamic behavior in turbulent flow is of great significance for controlling the bubble interface area and gas phase residence time. These parameters are key factors influencing heat and mass transfer efficiency and are crucial for device design. However, due to the instability of the turbulent flow field, bubble deformation, oscillation, coalescence and breakup, it is not as convenient to study the bubble behavior in turbulence as that in stagnant liquid, such as the rising characteristics of bubbles including the terminal velocity and trajectory in stagnant water [1–4]. However, heat and mass transfer in industrial devices often occur under turbulent conditions, the dynamics of single bubbles under turbulent conditions is of necessity.

Gas–liquid turbulent flow exhibits complex interfacial interactions. For example, in the turbulent boundary, the presence of bubbles has been demonstrated to have positive effect on drag reduction [5–7]. Extending to the bubble column, Zhou *et al.* [8] elucidated the dual effect of bubbles: enhancing the turbulence at a low gas void faction while suppressing it at a high gas void faction. The influence of the liquid on bubbles is directly manifested through the forces acting on the bubbles, which in turn determine their behavior. In stagnant water, the forces acting on bubbles are mainly buoyancy and drag forces. Aybers and Tapucu [9] investigated parameters such as the rising velocity, trajectory, and shape of bubbles of different sizes in stagnant water. Tomiyama *et al.* [10] further derived the terminal velocity equation of rising bubbles. Liu *et al.* [11] explored the relationship among bubble size, bubble shape and bubble rising path. However, bubbles in turbulent flow are subject to multiple forces, including inertial force, pressure gradient force, gravity force, drag force, virtual mass force, shear lift force and wall lift force, *etc.* [12]. However, researchers often neglect minor forces and focus on dominant ones for convenience. For example, Lane *et al.* [13] considered only drag force, added mass force, lift force and turbulent dispersion force acting on bubbles, and proposed a correlation for drag in a turbulent stirred tank. In the stirred tank, Li and Li [14] neglected the interactions between bubbles and focused on diffusion, shear production, pressure–strain correlation, dissipation and phase interaction terms for liquid and gas phase. They established a second-order gas–liquid two-phase turbulence model to predict the influence of operating parameters on bubble dynamics and liquid flow fields. However, existing turbulence models are all unable to fully predict the motion behavior of bubbles in turbulence and can only achieve partial success [15]. Therefore, it is necessary to study the motion of a single bubble in the turbulent flow, to reveal the characteristics of forces acting on bubbles.

In previous research, there are various apparatus to study the bubble motion including the mass transfer depending on the liquid flow pattern. In the stagnant water system, liquid tanks were always used to study the rise of bubbles, but finite device dimension limits the observation time of the bubbles. To extend the duration of observation, Lakshmanan *et al.* [16] proposed an improved setup with a rotating chamber to keep the bubbles relatively static. When studying the single bubble motion in turbulence, the key lies in the device that can not only capture the bubbles but also achieve sufficient observation time. Nate and Himmelblau [17] developed a funnel device introducing a liquid flow field from top to bottom, which can balance the fluid resistance and the buoyancy of the bubbles, thereby trapping single bubbles at high Reynolds numbers. Similarly, Vasconcelos *et al.* [18] used a Venturi tube to trap bubbles and explore the influence of surfactants on gas–liquid mass transfer. In our previous work [19–21], a cavity flow driven by a channel flow above was successfully utilized to confine bubbles within tens of seconds to study its mass transfer behavior.

In this work, the cavity flow driven by the channel flow above it is used to trap the bubbles in order to realize the bubble trajectory, residence time distribution and forces acting on bubble. The paper is organized as below: The trajectories of the bubbles under different flow conditions were observed by a high-speed camera. Additionally, particle image velocimetry (PIV) was employed to measure the average flow field, Reynolds stress ($\boldsymbol{\tau}$), energy dissipation rate (ε) and turbulent kinetic energy (k) of the liquid phase in the cavity under different channel flow rates. Then, the forces on the bubble were analyzed generally based on the average liquid-phase flow field, and the fluctuating velocity and turbulence time scale were also introduced to account for turbulence. The bubble trajectory and motion time could be obtained by calculating the forces on the bubble. In this paper, the motion characteristics and residence time distribution characteristics of bubbles in cavity flow driven by a turbulent channel are studied to grasp the forces on bubbles and the influence of these forces on the motion of bubbles. This lays the groundwork for calculating the mass transfer of bubbles in a cavity.

2. Experimental Setups and Methodology

2.1. Experimental apparatus and materials

The experimental setup which captures the bubble' motion in the cavity is shown in Fig. 1. The experimental apparatus consists of a flow channel (20 mm × 20 mm × 1200 mm, polymethyl methacrylate (PMMA)) with a cavity (60 mm × 80 mm × 6 mm, PMMA, see Fig. 2), a vessel containing liquid, a delivering pump for overall liquid circulation, a valve to control the flow, a flowmeter, a light emitting diode (LED) lamp (400 W) as light source, a chiller to control temperature, a high-speed camera (GO-5000-USB, JAI, DK) with a resolution of 2560 × 2048 pixels recording the bubble motion in the cavity, and a lens (AF MICRO 60 mm, Nikkor, Japan). The single bubbles are released at the bottom of the cavity by a microinjector.

An air–water system was used and all experiments were controlled at room temperature (25 °C ± 0.5 °C). A circulating flow was generated in the cavity so that a bubble released from the gas inlet was able to circulate in the liquid flow. In the experiments, the channel liquid volumetric flowrate (Table 1) under cases labeled 1–5 was controlled by a valve. The flow rate refers to the flow rate in the channel above the cavity. The volume, position, shape, and velocity of the bubble were determined through image analysis.

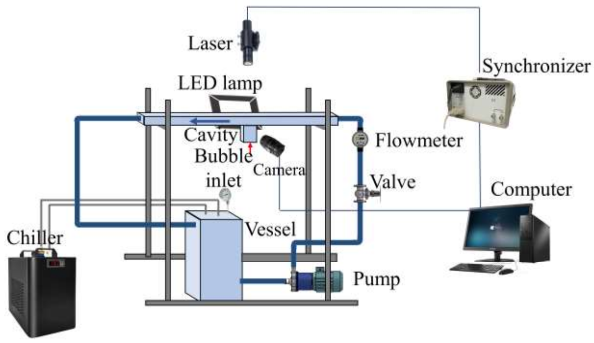

Fig. 1. Schematic diagrams of experimental apparatus.

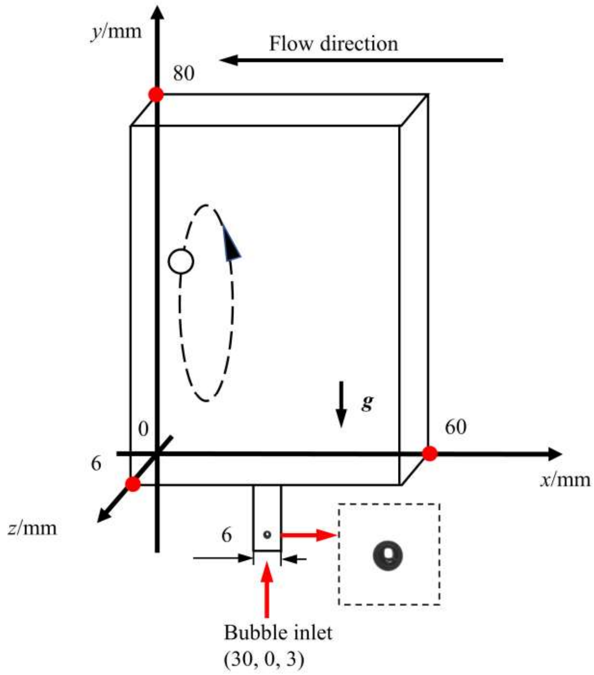

Fig. 2. Dimension of the cavity and bubble release location.

Table 1 Experimental conditions.

Case	Liquid flow rate from pump/L·min^{-1}	Re_L in the channel
1	24 ± 0.2	2.1×10^4
2	30 ± 0.2	2.7×10^4
3	36 ± 0.2	3.2×10^4
4	42 ± 0.2	3.7×10^4
5	48 ± 0.2	4.3×10^4

Re_L is the channel Reynolds number, $Re_L = d_c u_L \rho_L \cdot \mu_L^{-1}$. d_c is the equivalent diameter of the channel, which is 0.02 m. u_L is the liquid velocity in the channel, ρ_L is the liquid density, and μ_L is the liquid viscosity.

The water flow in channel and cavity as well as the bubble dynamics are governed by the following dimensionless numbers: the channel Reynolds number Re_L, Eotvos number Eo, Morton number M, and bubble Reynolds number Re. In our research, the definition and range of Re_L is shown in Table 1. $Eo = g(\rho_L-\rho_B)d_B^2\cdot\sigma^{-1}$, and the value is 0.50. $M = g(\rho_L-\rho_B)\mu_L^4\cdot(\rho^{-1}{}_L^{-2}\sigma^{-3})$, and the value is 2.4×10^{-11}. $Re = d_B u_s \rho_L\cdot\mu_L^{-1}$, and the value ranges from 100 to 500. σ is the surface tension of the liquid, ρ_B is the bubble density, d_B is the bubble diameter and u_s is the magnitude of the relative velocity of bubble and liquid.

2.2. PIV technique

A two-dimensional (x-direction and y-direction) particle image velocimetry (PIV) system was used to measure the liquid flow field in the cavity, see Fig. 1. The system comprised a laser (Dual Power 100_100 Laser 2×100 mJ), a CMOS camera (Speed Sense 4 MP, 2320 × 1720 pixels), a synchronizer (Dantec, DK), and a computer with software Dynamic Studio. The flow was seeded with hollow glass spheres with a nominal diameter of 10 μm. The laser light sheet had a thickness of approximately 1 mm in the z-direction and was placed in the middle of the cavity at z=3 mm. Considering the scattering performances of particles and PMMA reflection, the physical dimensions of the acquired PIV images were reduced, resulting in a captured area of 58 mm × 68 mm.

The time interval Δt between two successive laser pulses for each pair of images was 250 μs. The PIV measurements were conducted at the frequency of 85 Hz. One thousand pairs of images at each flow case (see Table 1) were captured to ensure statistical stability of the mean velocity of the liquid, which limited the total acquisition time to 11.8 s. A cross-correlation algorithm was applied using interrogation windows of 32 pixel × 32 pixel with 50% overlap.

2.3. Bubble imaging analysis methods

A high-speed camera was utilized to capture the motion of a single bubble. The images were analyzed using MATLAB software (MATLAB 2020b, USA). Fig. 3 presents a flowchart illustrating the image processing steps involved in this analysis. The process consisted of denoising, median filtering, edge detection, bubble area filling, binarization, and obtaining the centroid coordinate and the equivalent diameter of the bubble [20,21].

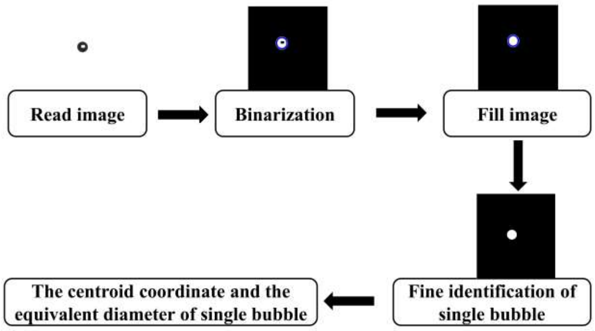

Fig. 3. Bubble image processing flow sheet.

A 5 µl microinjector with the inner diameter of 0.3 mm was utilized to release the equally sized bubbles. In each experiment, single bubble is released into the cavity and the behavior of the bubble is observed and recorded. After the bubble left the cavity, wait 5 min before releasing next bubble. The specific release position and initial morphology of the bubbles are also shown in Fig. 2**.** The bubble size was determined by processing the images using MATLAB, following the steps outlined in Fig. 3. The equivalent diameters of single bubbles (d_B) in 10000 experimental pictures were counted, see Fig. 4. The majority of bubbles had a mean equivalent diameter of 1.92 mm, with a deviation of ± 5%. The volume of the bubble was calculated using MATLAB based on its projected area in the *z*-plane [20,21]. As we will see later in Section 4.2.2, bubbles deform during their trajectory in the cavity with consequences for the hydrodynamic forces they experience, particularly the lift force.

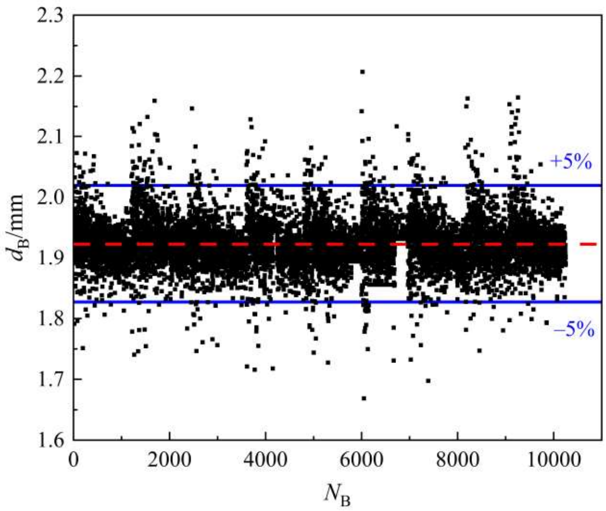

Fig. 4. Equivalent diameter of bubbles d_B *vs* the bubble number N_B.

Only a fraction of the injected single bubbles was retained within the cavity, while the rest escaped right after injection. The residence time of single bubbles was defined as the duration from the bubble release to exit. Turbulence makes that the flow field in the cavity is continuously changing over time, leading to varying impacts on each bubble, which results in different residence times of individual bubbles. Therefore, we derived a residence time distribution from the experimental data. The mean residence time was calculated for varying numbers of bubbles, and convergence was observed when the number of bubbles exceeded 160, see Fig. 5. In subsequent experiments, the residence time of 200 bubbles was recorded under each experimental condition to determine the mean residence time.

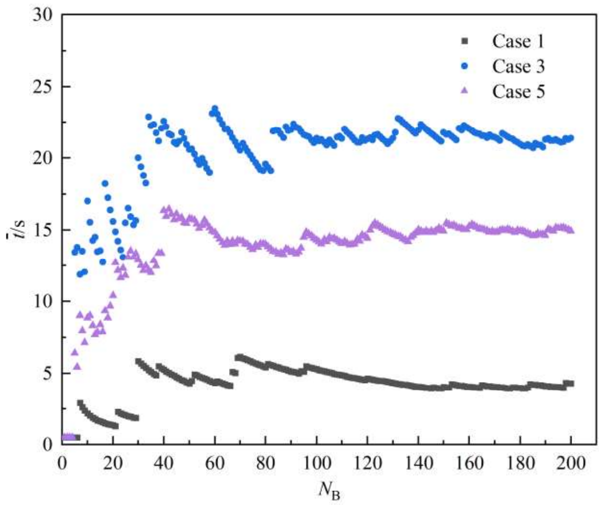

Fig. 5. Convergence of mean residence time $\bar{t}$ with bubble number N_B.

During the experiment, if the bubbles circulate in the cavity, we record the motion of bubbles for 20 s at 60 frames per second. A set of experimental data from Case 2 is used as an example to show how to obtain the mean bubble trajectory, see Fig. 6(a). Firstly, take the average of all bubble centroid coordinates in the images. Secondly, using the average as the center point (origin), the coordinates of the bubble's centroid were converted from a cartesian coordinate system to a polar coordinate system. Thirdly, the polar coordinates were segmented into intervals of 5 degrees, and each interval's coordinates were averaged to obtain the average coordinate for that interval, see Fig. 6(b). A total of 72 points were obtained, which constituted the average bubble trajectory of the experiment. Finally, convert 72 points coordinates to a cartesian coordinate system, see Fig. 6(c).

Due to the stochastic nature of bubble motion, averaging was performed separately for 1, 3, 5, 7, and 9 bubbles. The trajectories from these experiments showed significant overlap, see Fig. 7. Therefore, in subsequent trajectory analyzes, 10 bubble experiment trajectories in each case were randomly selected as samples.

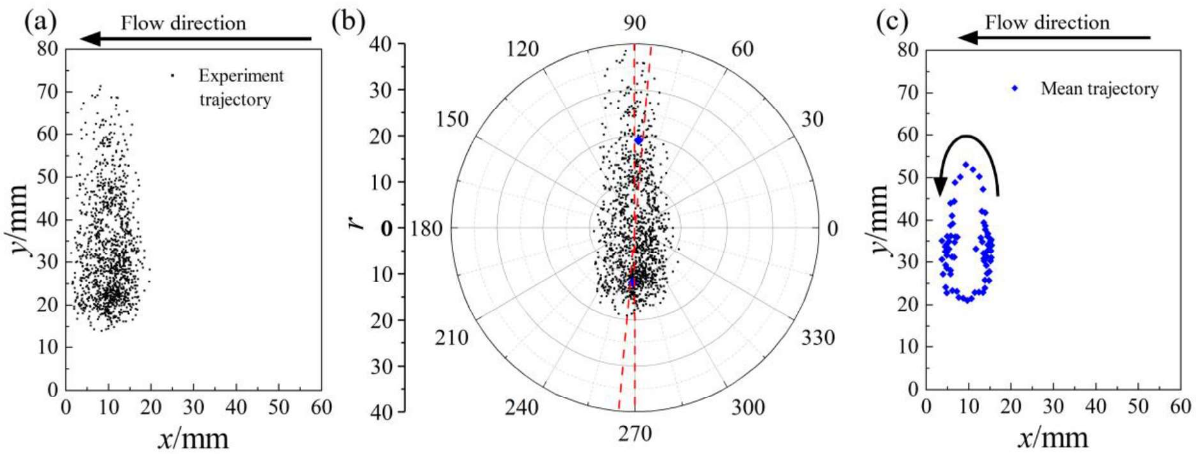

Fig. 6. Bubble trajectories for one set for Case 2: (a) bubble centroid coordinates in a Cartesian coordinate system, (b) bubble centroid coordinates in a Polar coordinate system, (c) mean bubble trajectory in a Cartesian coordinate system.

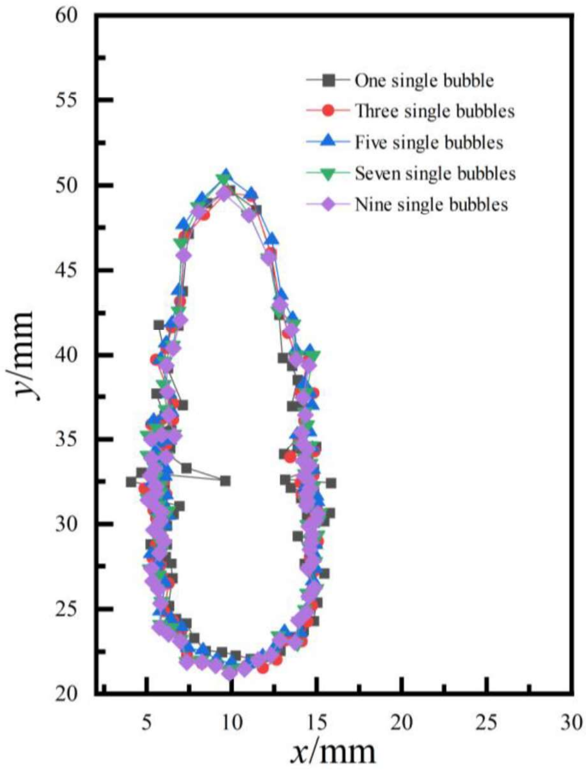

Fig. 7. Bubble mean trajectories for 1, 3, 5, 7, and 9 single bubbles for Case 2.

To further investigate the influence of the bubble release position on the bubble trajectory, the release point of bubbles was set at points A, B and C below the cavity, respectively, see Fig. 8. It was observed that the average trajectory of bubbles remained the same regardless of the release point.

Point B was selected as the release point for all subsequent experiments.

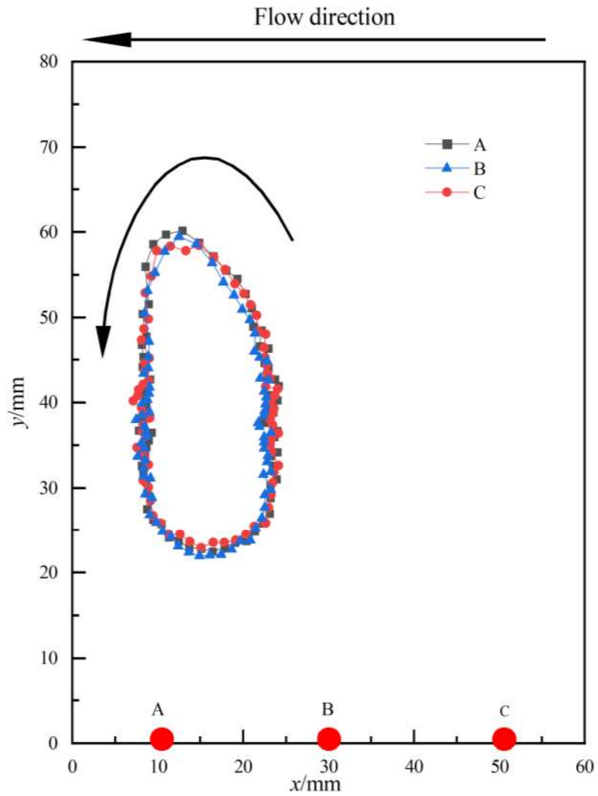

Fig. 8. Bubble mean trajectories when the bubbles were released from different positions A, B or C.

3. Theoretical Calculation of Bubble Motion

3.1. Framework

In the theoretical calculation of bubble motion, the flow field data used is derived from 2D-PIV experiments. These experiments provide the values of average liquid velocity ($\overline{\boldsymbol{u}_{\mathrm{L}}}$), liquid-root-mean square velocity ($\boldsymbol{u}_{\mathrm{L,rms}}$), turbulence kinetic energy (k), Reynolds stress ($\boldsymbol{\tau}$) and turbulent dissipation rate (ε) on a two-dimensional square grid with spacing 1.62 mm.

Since the experiment uses a two-dimensional PIV system, which lacks velocity information in the z-direction, isotropic assumptions are made, that is, the fluctuating velocity in the z-direction is estimated from the fluctuating velocity in the other two directions [22,23] (please refer to the supplementary materials for further details of the isotropic assumption). It should be noted that the isotropic turbulence assumption may introduce certain uncertainties. Due to the confinement in z-direction, this assumption may overestimate the velocity fluctuations in z-direction. This leads to deviations in the estimation of turbulence kinetic energy and an overestimation of the forces acting on the bubble. However, given the quasi-two-dimensional design of the cavity and the supporting PIV results, this assumption is considered acceptable within the accuracy required for the present analysis. Therefore, k is expressed as:

$$k = \frac{3}{4}(u_{\mathrm{L,rms},x}^2 + u_{\mathrm{L,rms},y}^2) \tag{1}$$

When the spatial resolution of the vectors is not sufficient to accurately calculate ε, a large eddy PIV method is used to calculate ε, taking advantage of the similarity between PIV and large eddy simulation methods [24]. Based on the eddy viscosity model proposed by Smagorinsky [25], the assumption $\left\langle \left(s_{ij}s_{ij}\right)^{3/2} \right\rangle = \left(\overline{s_{ij}s_{ij}}\right)^{3/2}$ [26], and the isotropic assumption, ε is expressed as [27,28]:

$$\varepsilon = C_{\mathrm{S}}^2 \Delta^2 \left\{ \frac{3}{2}\overline{\left(\frac{\partial u_{\mathrm{L},x}}{\partial x}\right)^2} + \frac{3}{2}\overline{\left(\frac{\partial u_{\mathrm{L},y}}{\partial y}\right)^2} + 3\overline{\left(\frac{\partial u_{\mathrm{L},x}}{\partial y}\right)^2} + 3\overline{\left(\frac{\partial u_{\mathrm{L},y}}{\partial x}\right)^2} \right\} \tag{2}$$

C_{S} is the Smagorinsky–Lilly constant which depends on the degree of windows overlap and the value of which is 0.19 [27,28], Δ is the size of the interrogation window, and s_{ij} is the resolved strain-rate tensor.

The calculation procedure for bubble motion is shown in Fig. 9. The bubble is released at the initial position (x = 30 mm, y = 5 mm), which is close to point B, see Fig. 8. The average liquid velocity ($\overline{\boldsymbol{u}_{\mathrm{L}}}$) at the bubble position obtained by linear interpolation, plus a random liquid velocity ($\boldsymbol{u}_{\mathrm{L}}'$), is used as the liquid velocity for calculations. The force on the bubble is calculated according to the bubble velocity and flow field data, see Section 3.2. The acceleration of the bubble is calculated based on Newton's second law. The time interval Δt used for calculation is 0.001 s, and the velocity and the updated position of the bubble is obtained. The code is run 200 times for each case, and the number of calculation steps set by each run of the code is 300000.

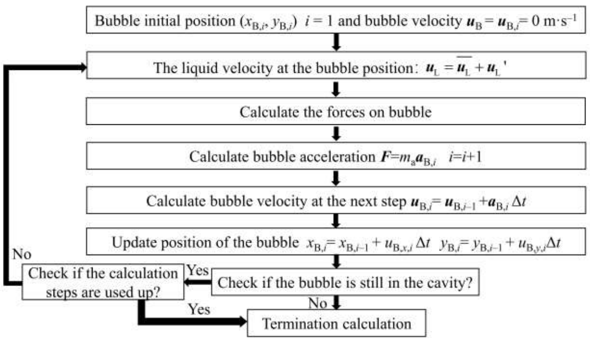

Fig. 9. Time stepping process for calculating bubble trajectory.

To include turbulence in our bubble motion calculation, the determination of instantaneous liquid velocity is important. The liquid velocity used in the simulation is equal to $\overline{\boldsymbol{u}_{\mathrm{L}}}$ plus a fluctuating velocity ($\boldsymbol{u}_{\mathrm{L}}'$). Here the fluctuating velocity $\boldsymbol{u}_{\mathrm{L}}'$ can be expressed by a random number (a) multiplied by the root-mean-square velocity $\boldsymbol{u}_{\mathrm{L,rms}}$. The distribution of a follows a standard normal distribution that has average 0 and standard deviation 1 that for numerical reasons we cut off at an absolute value of 8; *i.e.* a is in the range [–8, 8]. The turbulence time scale (t_{ts}) is the characteristic time over which turbulent eddies or fluctuations in a fluid flow retain their coherence before dissipating or losing their identity, and is expressed as [29]:

$$t_{\mathrm{ts}} = 0.16\frac{k}{\varepsilon} \tag{3}$$

To characterize the variation of turbulence in the cavity, t_{ts} is incorporated into simulation. At the beginning of the simulation, we create a fluctuating velocity for calculation and record the bubble residence time (t_{res}). When t_{res} exceeds t_{ts} at the bubble release position or t_{res} exceeds t_{ts} at the current position of the bubble, we update the fluctuating velocity and record t_{res} starting from 0. At this time, the t_{ts} at that position is used to compare with t_{res}. We continue the calculation until again t_{res} exceeds the t_{ts}, update the fluctuating velocity and record t_{res} starting from 0 and so on.

3.2. Forces on the bubble

According to Newton's second law, the equation of motion of the bubble reads

$$\left(m+m_{\mathrm{a}}\right)\mathrm{d}\boldsymbol{u}_{\mathrm{B}} / \mathrm{d}t = \sum \boldsymbol{F} - mg\boldsymbol{e}_y \tag{4}$$

$$m = \frac{\pi}{6} d_{\mathrm{B}}^3 \rho_{\mathrm{B}} \tag{5}$$

$$m_{\mathrm{a}} = \frac{\pi}{12} d_{\mathrm{B}}^3 \rho_{\mathrm{L}} \tag{6}$$

g is the gravitational acceleration, $\boldsymbol{e}_y$ is the unit vector in vertical (y) direction, ρ_{B} is the bubble density, m_{a} is the added mass, m is the bubble mass and $\sum \boldsymbol{F}$ is the sum of forces acting on the bubble. Clearly, since ρ_{L} is much higher than ρ_{B}, the added mass m_{a} [30] is much larger than the mass m of the bubble itself, so m is ignored.

Liquid velocity is equal to average liquid velocity plus a fluctuating velocity:

$$\boldsymbol{u}_{\mathrm{L}} = \overline{\boldsymbol{u}_{\mathrm{L}}} + \boldsymbol{u}_{\mathrm{L}}' \tag{7}$$

The sum of forces is expressed as:

$$\sum \boldsymbol{F} = \boldsymbol{F}_{\mathrm{D}} + \boldsymbol{F}_{\mathrm{P}} + \boldsymbol{F}_{\mathrm{L}} \tag{8}$$

$\boldsymbol{F}_{\mathrm{D}}$ is the drag force, $\boldsymbol{F}_{\mathrm{L}}$ is the lift force, and $\boldsymbol{F}_{\mathrm{P}}$ is the pressure gradient force. All forces are 2-dimensional, since the forces are calculated based on the 2-dimensional liquid flow field obtained by PIV.

The drag force is due to the resistance experienced by a bubble moving in the liquid. The drag force is expressed as

$$\boldsymbol{F}_{\mathrm{D}} = \frac{1}{8}\pi d_{\mathrm{B}}{}^{2}\rho_{\mathrm{L}}C_{\mathrm{D}}\,|\,\boldsymbol{u}_{\mathrm{L}} - \boldsymbol{u}_{\mathrm{B}}\,|\,(\boldsymbol{u}_{\mathrm{L}} - \boldsymbol{u}_{\mathrm{B}}) \tag{9}$$

where for the drag coefficient C_{D}, the model of Tomiyama *et al.* [31] has been used:

$$C_{\mathrm{D}} = \max\left\{\frac{24}{Re}\left(1 + 0.15Re^{0.687}\right), \frac{8}{3}\frac{Eo}{Eo+4}\right\} \tag{10}$$

The dimensionless numbers Re and Eo have been introduced in Section 2.1. The specific drag force correlation (Eq. (10)) is for what Tomiyama *et al.* [31] call a “contaminated system”. We have tested the performance of this correlation by measuring the terminal rise velocity of an air bubble of diameter of 3.0 mm in stagnant water. The result of this experiment – a velocity of 0.30 $\mathrm{m\cdot s^{-1}}$ – implies a drag coefficient of $C_{\mathrm{D}} = 0.43 \pm 0.02$ where Eq. (10) predicts $C_{\mathrm{D}} = 0.44$.

The lift force acting on the bubble comes from the velocity gradient of the liquid phase and the relative velocity between the gas and liquid phases. The lift force is expressed as [32,33]:

$$\boldsymbol{F}_{\mathrm{L}} = \frac{1}{6}\pi d_{\mathrm{B}}{}^{3}\rho_{\mathrm{L}}C_{\mathrm{L}}\left(\boldsymbol{u}_{\mathrm{L}} - \boldsymbol{u}_{\mathrm{B}}\right)\times\left(\nabla\times\boldsymbol{u}_{\mathrm{L}}\right) \tag{11}$$

Details of the lift force coefficient C_{L} will be discussed in Section 4.2.2.

The pressure gradient force has two contributions: (1) the buoyancy force is the result of the hydrostatic pressure gradient that would also be present in the absence of a background flow; (2) the pressure gradient that is the result of the background flow. The pressure gradient is estimated from the steady Reynolds-averaged Navier–Stokes equation that we write in the following form:

$$\nabla p = -\rho_{\mathrm{L}}\boldsymbol{u}_{\mathrm{L}}\cdot\nabla\boldsymbol{u}_{\mathrm{L}} + \mu_{\mathrm{L}}\nabla^{2}\boldsymbol{u}_{\mathrm{L}} - \rho_{\mathrm{L}}g\boldsymbol{e}_{y} + \nabla\cdot\boldsymbol{\tau} \tag{12}$$

$\boldsymbol{\tau}$ is the Reynolds stress tensor and $\boldsymbol{e}_{y}$ is unit vector. In two dimensions, it reads

$\boldsymbol{\tau} = \begin{bmatrix} -\rho\overline{u_x'u_x'} & -\rho\overline{u_y'u_x'} \\ -\rho\overline{u_x'u_y'} & -\rho\overline{u_y'u_y'} \end{bmatrix}$. It has been calculated from the fluctuating velocities in our PIV data sets. Comparison of the contributions to the pressure gradient of $-\rho_\mathrm{L}\boldsymbol{u}_\mathrm{L}\cdot\nabla\boldsymbol{u}_\mathrm{L}+\mu_\mathrm{L}\nabla^2\boldsymbol{u}_\mathrm{L}$ on one side and of $\nabla\cdot\boldsymbol{\tau}$ on the other shows that the latter are smaller than the former by three orders of magnitude at least so that the $\nabla\cdot\boldsymbol{\tau}$ contribution has been neglected. The pressure gradient force is thus calculated according to

$$\boldsymbol{F}_\mathrm{P} = -\frac{\pi}{6}{d_\mathrm{B}}^3(-\rho_\mathrm{L}\boldsymbol{u}_\mathrm{L}\cdot\nabla\boldsymbol{u}_\mathrm{L}+\mu_\mathrm{L}\nabla^2\boldsymbol{u}_\mathrm{L}-\rho_\mathrm{L}g\boldsymbol{e}_y) \tag{13}$$

As is clear, the part $\frac{\pi}{6}{d_\mathrm{B}}^3\rho_\mathrm{L}g\boldsymbol{e}_y$ represents the buoyancy force and $-\frac{\pi}{6}{d_\mathrm{B}}^3(-\rho_\mathrm{L}\boldsymbol{u}_\mathrm{L}\cdot\nabla\boldsymbol{u}_\mathrm{L}+\mu_\mathrm{L}\nabla^2\boldsymbol{u}_\mathrm{L})$ is the part induced by the background flow.

In Eq. (4), we neglect the term $mg\boldsymbol{e}_y$ as it is (in an absolute sense) much smaller than the buoyancy force.

4. Results and Discussion

4.1. Experimental results and discussion

4.1.1. Residence time of single bubbles

We analyze the motion time of all the bubbles under different liquid flow rates, and the time required for a bubble to leave the cavity directly upon release is 0.5 s. Fig. 10(a) shows the distribution of bubble residence time (t_res) for different cases, the residence time of most bubbles is less than 60 s. In Case 2 and Case 3, the residence time of some bubbles is longer. The probability of bubbles having a residence time more than 0.5 s increases with the increase of flow rate, see Fig. 10(b). In Case 1, bubbles are difficult to be trapped in the cavity, and the residence time of bubbles is short. The probability of bubbles with residence time higher than 0.5 s affects the mean residence time of bubbles ($\bar{t}$). The mean residence time of bubbles increases first and then decreases with the increase of flow rate, see Fig. 10(c). The decrease in $\bar{t}$ is due to the relatively short residence time of individual bubbles, despite the high probability of bubbles with residence time higher than 0.5 s in Case 4 and Case 5. There is a range of flow rates where the bubbles are trapped in the cavity for a relatively long time.

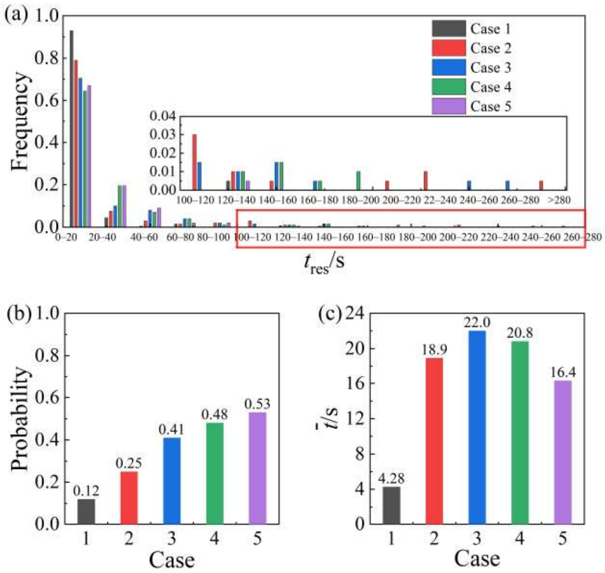

Fig. 10. Residence characteristics of bubbles per case: (a) distribution of residence time, (b) probability of bubbles having a residence time over 0.5 s, (c) mean residence time.

4.1.2. Trajectories of single bubbles

One of the controlled variables is the liquid flow rate, which directly alters the flow field in the cavity, and, as a result, influences the bubble motion. Fig. 11 shows the average flow fields of the liquid phase obtained by the PIV technique. The fluid flows from right to left in the channel. A vortex forms in the cavity. Three regions of high velocity are observed near the left and right side walls and at the bottom and the velocity maxima in all three regions increase with the increase of the channel flow rate. Fluid from the right side enters the cavity and strikes the left side of the wall, and generates large downward velocities. Some kinetic energy is lost at the bottom and the right side, leading to the highest liquid velocity in the left region. With the increasing channel flow rate, the flow field distribution in the cavity shows little variation, although the overall liquid velocity increases. The area of the asymmetric low-velocity vortex core inside the cavity becomes smaller while maintaining its overall shape. Given the results of turbulent kinetic energy k in Fig. 12, it's clear that the flow in the cavity is turbulent for all cases. Generally, the strongest turbulence is in the top-left corner of the cavity and the weakest in the middle of the cavity.

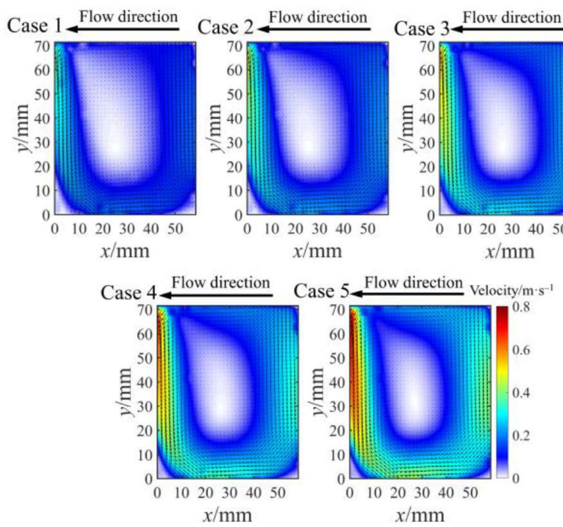

Fig. 11. Average flow fields of liquid phase in the cavity per case.

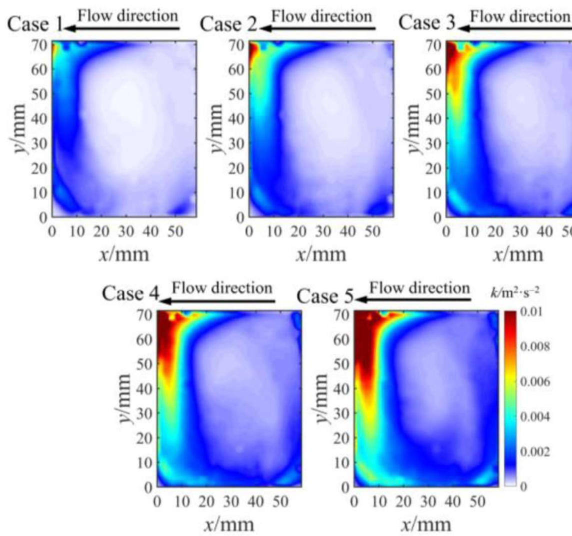

Fig. 12. Turbulent kinetic energy *k* distributions in the cavity per case.

The bubble motion in the cavity is directly affected by the liquid-phase flow field. A scatter density plot of instantaneous bubble centroid location of 10 sets of experiments (one bubble for each set) in each case was generated to illustrate the probability distribution of bubble positions within the cavity, see Fig. 13.

Each density plot contains 10000 bubble centroid coordinates (10 bubbles × 1000 instantaneous centroid coordinates per bubble), that is to say, the color plots represent the ratio of the number of bubbles occurrence in a specific area (0.46 mm × 1.01 mm) divided by the total bubble centroid coordinates (10000). Generally, bubbles predominantly appeared in the left half of the cavity ($x < 30$ mm). At low flow rates, the bubble trajectory points are mainly concentrated in the left and bottom halves of the cavity, with fewer occurrences in the upper part. As the flow rate increases, the distribution of bubble trajectory points becomes more uniform, expanding the overall motion range within the cavity while still predominantly favoring the left side. The bubble distribution of Case 3 shows the most uniform distribution across different *y* positions. Case 5, with the highest flow rate, displays the broadest range of in *x*-direction bubble motion compared to other cases.

To represent the variation in bubble trajectories under different channel flow rates, the average trajectory of bubbles according to the procedure explained in Section 2.3.4 in different cases are presented in Fig. 14. As the flow rate in the channel increases, the coverage area of bubble trajectories expands, shifting towards the right and upward, and closer to the area with the lowest liquid velocity in the center of the cavity.

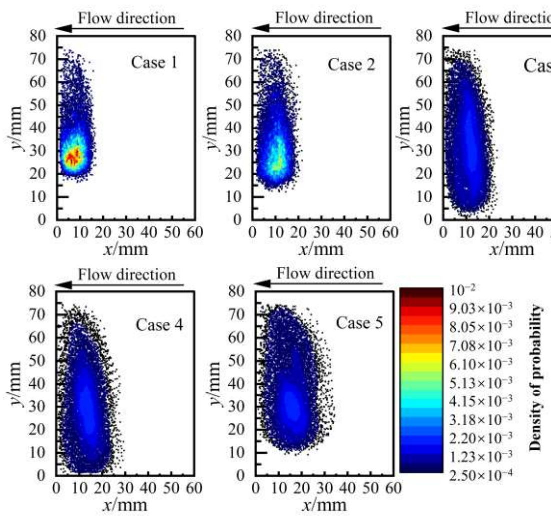

Fig. 13. Probability density of bubble centroid coordinates per case (white means no bubble observed).

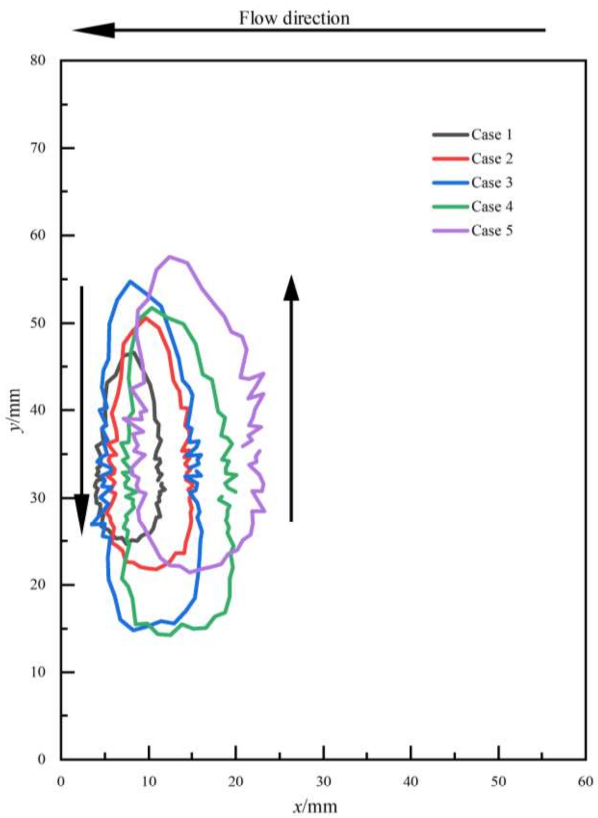

Fig. 14. Mean trajectories of bubbles' motion per case.

With the increase of flow rate, single bubbles are more likely to move to the upper left corner of the cavity. It can be seen from the experimental data that in the upper left corner of the cavity, a part of the fluid exits while new fluid enters, which results in a significantly larger k there than elsewhere, see Fig. 12. Larger liquid velocity enhances the downward liquid flow velocity within the area covering the bubble motion, facilitating trapping of bubbles within the cavity. Simultaneously, higher liquid velocity in the upper part of the cavity due to higher channel flow, induces stronger turbulence in the upper left corner. This stronger turbulence increases the likelihood of bubbles being carried away from the cavity by the departing liquid. Thus, changes in flow rate alter the liquid flow field in the cavity, which in turn affects bubble trajectories, ultimately affecting the mean residence time of bubbles.

4.2. Calculation results and discussion of bubble motion

As discussed in Section 4.1, the experimental results show that the bubble motion and residence time in the cavity are strongly influenced by the liquid flow rate and turbulence characteristics. With the increase of the channel flow rate, the bubble trajectories expand towards the central region of the cavity, while the mean residence time exhibits a non-monotonic trend. Because the cavity has a small depth of 6 mm, the bubble motion can be effectively represented using a quasi-two-dimensional cavity model, which can help establish a quantitative understanding of the bubble behavior. The liquid velocity, turbulent kinetic energy, and energy dissipation rate in cavity obtained by PIV were directly used as inputs to the model, ensuring that it represents the actual flow conditions within the cavity rather than relying on assumed flow structures.

4.2.1. Discussion of C_D

In the calculation of the forces acting on bubbles, the required liquid flow field information and bubble diameter and other data can be obtained from the experimental test. However, the drag coefficient C_D and lift coefficient C_L cannot be determined from experimental results; it is necessary to select appropriate models for them. Case 3 is taken as an example for this selection.

Although the drag coefficient model for single bubbles, as proposed by Tomiyama *et al.* [31] was derived in stagnant water, they also discussed the application of the drag coefficient model in the motion of single bubbles under a micro or zero gravity condition in a pipe flow. In the literature [31], the liquid Reynolds number of the tube flow is between 10–10^6, corresponding to a liquid velocity between 0.00033 and 33.3 $m \cdot s^{-1}$. Thus, while it was originally derived under stagnant water conditions, it is not confined to stagnant water systems. Instead, it provides a model in an applicable range which relates to bubble dimensionless numbers ($10^{-2} < Eo < 10^3$, $10^{-14} < M < 10^7$, $10^{-3} < Re < 10^5$). In this research, Eo is 0.50 ± 0.05, M is 2.4×10^{-11}, and the range of Re is 100–500, which makes the model suitable. Although the Tomiyama model is suitable for our case, we check the sensitivity of C_D on bubble motion, while for now, we set the commonly accepted value of 0.5 for C_L [34,35].

Based on the experimentally obtained data, which were brought into Eq. (10), it was found that the range of instantaneous C_D during bubble motion is from 0.5 to 1.25. In order to assess the effect of C_D on bubble motion, we changed C_D in the range [0.5, 3] which covers the range of C_D calculated based on the model of Tomiyama *et al.* [31]. With these values, all bubbles left the cavity directly, and therefore the calculation results were inconsistent with the experimental results. The trajectory plots of 20 of these bubbles were shown for different C_D in Case 3, see Fig. 15. So, next we discuss the effect of C_L on the bubble motion.

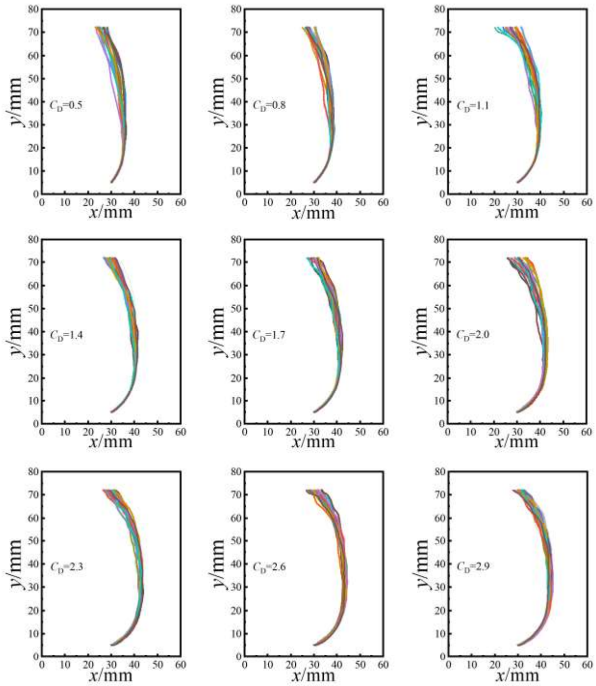

Fig. 15. Bubbles' trajectories when C_D is varied and $C_L = 0.5$ for Case 3.

4.2.2. Discussion of C_L

Most models of the lift coefficient as used in Eq. (11) are available for stagnant water and low Reynolds number, with a value of $C_L = 0.5$ [36], while the presence of cylinder wake in bubble motion can further increase the lift coefficient [37]. In addition to studies on bubbles in stagnant water, there are also literatures that study the bubble motion in the turbulent flow. However, they mainly focus on bubble swarms in the bubble column and pipe [38–42]. The lift coefficient models of bubble swarms in turbulent flow are applied in our systems and it is found that the values of C_L are between 0.25 and 0.6. In addition, these models are not directly related to bubble deformation. Adoua *et al.* [43] investigated the change of bubble lift as a result of deformation in a shear flow, and found that the lift coefficient increases with the increase of bubble aspect ratio χ (the ratio of the major axis length to the minor axis length). The lift coefficient model proposed by Adoua *et al.* [43] is expressed as:

$$C_L = 0.5 + 0.612(\chi - 1) \tag{14}$$

This model is applicable to our system. Existing literature shows that bubbles with diameters smaller than 2–3 mm behave as rigid spheres with immobile interfaces in stagnant water [44]. When Kure *et al.* [45] studied the motion of carbon dioxide bubbles less than 3 mm in diameter in stagnant water, they assumed that the bubbles were rigid. Bubbles smaller than 2 mm in diameter behave as rigid spheres in stagnant water. However, we observed that bubbles undergo continuous deformation in turbulence and χ is continuously changing, see Fig. 16. Several recent studies have investigated the influences of bubble deformation on the lift force. Hessenkemper *et al.* [46] experimentally examined the effects of bubble size on the lift coefficient for ellipsoidal bubbles rising in water, providing an initial insight into how deformation modifies lift force. Zand *et al.* [47] further extended this understanding by demonstrating that bubble deformation altered the local vorticity distribution around the bubble, and the resulting imbalance in this vorticity governs both the magnitude and direction of the lift force. Their numerical simulations revealed a strong correlation between the vorticity generation rate and the bubble's lateral accelerations. Ziegenhein *et al.* [48] generated a controlled shear flow using a bubble plume to investigate single-bubble lift in an air–water system. They successfully quantified the relationship between bubble deformation, shear rate, and the lift coefficient. And they showed that the lift force varied strongly with the bubble aspect ratio and can even change sign when deformation becomes significant. Based on the experimentally obtained bubble aspect ratios, which were brought into Eq. (14), it was found that the range of C_{L} is from 0.5 to 1. Since our model does not keep track of bubble deformation, we reverted to defining an effective lift coefficient. For determining the effective lift coefficient, we use the experimentally observed mean residence time and probability of bubbles having a residence time more than 0.5 s. In order to determine effective C_{L}, calculations were carried out with C_{D} as in Eq. (10) and by varying C_{L} until they match the experimentally observed results.

The calculations showed that as C_{L} increases, the probability of bubbles having a residence time more than 0.5 s also increases, and the results for different cases are shown in Fig. 17. For example, for Case 3, it can be seen from Fig. 10(b) that the probability of bubbles having a residence time more than 0.5 s is 0.41. In the calculation, the closest matching probability is 0.45 and the corresponding value of C_{L} is 2.4. Then we propose 2.4 as the effective C_{L} for Case 3. This way we demonstrated that under turbulent conditions, the effective C_{L} ranging from 1.5 to 2.5 can show more realistic bubble behavior induced by bubble deformation. There may be other unknown factors at play, such as the bubble Reynolds number [32,49] and the wall effect [50,51], which affect the C_{L} value, resulting in the final obtained effective C_L different from the value obtained based on the model of Adoua *et al.* [43].

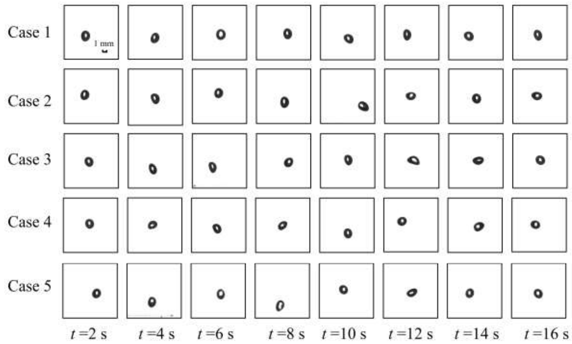

Fig. 16. Experimental images of bubbles deformation over time. $\chi \in [1, 1.8]$.

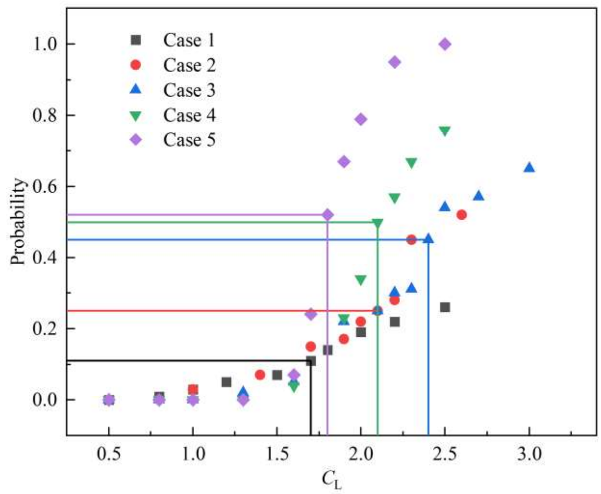

Fig. 17. Probability of bubbles with residence time more than 0.5 s for different C_L. The solid line is the value of effective C_L for the calculation when the calculated probability closest to the experimental probability per case.

The effective C_L first increases and then decreases with the increasing liquid flow rate, see Fig. 17. This behavior does not fully align with the general expectations that the higher the liquid flow rate, the stronger the turbulence, and the more severe the bubble deformation. The increase in flow velocity enhances local turbulence and wall-induced shear, thereby altering the vorticity field. The combined effects of the resulting asymmetric vorticity and the deformation-induced vorticity may lead to changes of the lift force acting on the deformed bubble, thereby affecting the bubble motion. This is consistent with the mechanism described by Zand *et al.* [47]. The PIV results (see Fig. 12) reveal strong spatial variations in turbulence intensity, with a highest turbulence near the left wall and a weaker turbulence toward the cavity center. This inhomogeneity of turbulence alters the local velocity gradients acting on the bubble under different liquid flow rate. As a result, the effective C_L first increases and then decreases with the increasing flow rate. In addition, near the left wall, wall-induced shear enhances the lateral velocity gradient and amplifies the lift force. At higher flow rates, single bubbles tend to migrate toward the cavity center, where wall influence weakens, leading to a reduction in the effective C_L. Therefore, the non-monotonic variation of the effective C_L with flow rate is a complex interaction among bubble deformation, turbulence, and wall effects. The effective lift coefficient obtained in this study serves as a parameter that integrates these coupling mechanisms. Although this empirical approach allows good agreement between the simulated and experimental results, it also remains limitation that it cannot directly resolve the instantaneous lift coefficient which might change along with bubble surrounding flow field and bubble deformation during its motion.

Taking Case 3 as an example, the bubble position and mean residence time were calculated with C_D as in Eq. (10) and varying C_L. 10 single bubble trajectories were randomly selected for different cases to obtain the scatter density plot, see Fig. 18. The calculated scatter plots are similar to the experimental scatter plots as shown before in Fig. 13. Changing C_L has little effect on the position distribution of bubbles motion.

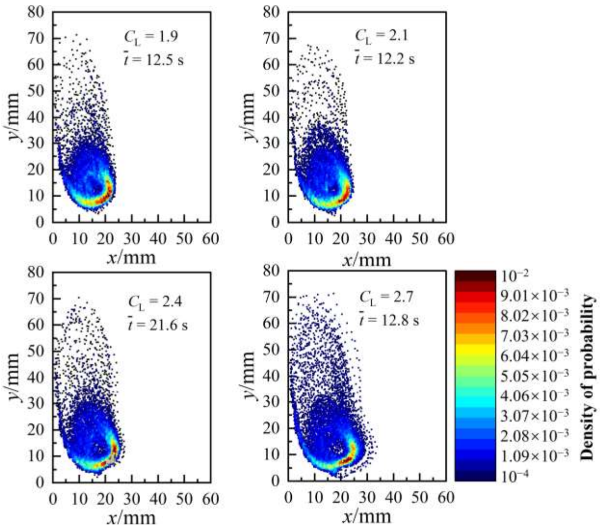

Fig. 18. Probability density of bubble centroid coordinates for changing C_L for Case 3.

4.2.3. Results of bubble motion calculation

The code used to calculate the bubble motion is executed by MATLAB software (MATLAB 2020b, USA) and the calculation results are shown in Table 2. The parameters affecting bubble motion include the lift coefficient (C_L), the drag coefficient (C_D), and the fluctuating liquid velocity ($\boldsymbol{u}_L'$). The value of C_D is computed according to Eq. (10) and $\boldsymbol{u}_L'$ is randomly generated with a standard deviation that depends on k. Since the bubble experiences continuous deformation during motion, in reality, C_L is not a constant value. Instead, in the calculations we adjusted C_L to match the experimentally obtained probability of bubbles having a residence time more than 0.5 s. Once this effective C_L was found, it was applied to the bubble motion calculation. The agreement between calculated and observed trajectories demonstrated the validity of the method we used. Although the turbulence in the cavity intensifies with the increase of liquid flow rate, bubble deformation does not necessarily increase continuously due to the bubble trajectories. At high liquid flow rates, the overall deformation tends to decrease as the bubble moves away from the left side wall. Therefore, the effective C_L exhibits a trend of first increasing and then decreasing as the liquid flow rate increases. The bubble positions were calculated, and 10 single bubbles were randomly selected for different cases to obtain the scatter density plots in Fig. 19. Comparing Fig. 13 and Fig. 19, the calculated results are reasonably consistent with the experimental results: the distribution range of the bubble positions in the cavity is similar to the experimental results; the distribution range of the calculated bubble positions expands with the increase of liquid flow rate, and the overall positions of bubbles also move upwards. This is similar to the experimental results. The maximum probability density of the calculated results is similar to the experimental results, and the positions of the maximum are similar as well.

The present model uses an effective lift coefficient to reproduce experimental bubble trajectories and residence times. Its applicability is primarily confined to quasi-two-dimensional cavity flows where the bubble diameter is small and the liquid-phase flow field can be accurately captured by PIV. Under these conditions, the effective C_L reasonably represents the combined effects of bubble deformation, turbulence isotropy, and wall effects. However, the generalization of this model is constrained by several factors. When the cavity depth increases and the flow becomes three-dimensional, the assumptions of isotropic turbulence may fail to hold. Similarly, in the case of larger bubbles or systems with multiple interacting bubbles, deformation and wake interactions are likely to dominate the lift dynamics in ways that fall outside the scope of the current model. Similarly, for larger bubbles or bubble cluster, the interaction between deformation and wake may make the current model no longer applicable.

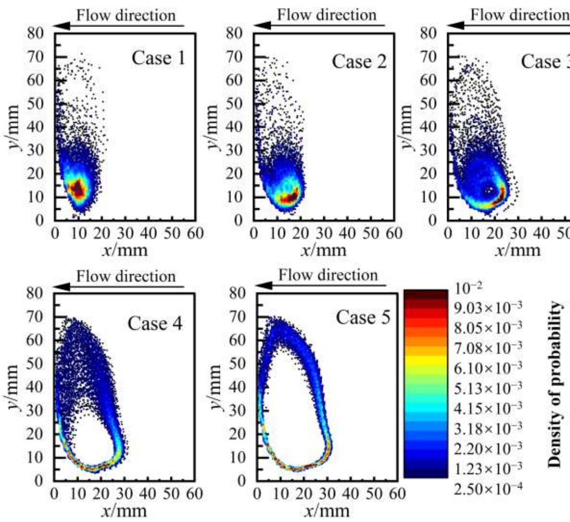

Fig. 19. Probability density of bubble centroid coordinates per case in the calculation.

Table 2 Calculated and experimental results.

Case	Probability of bubbles having a residence time more than 0.5 s by experiments	Experimental measured mean residence time/s	Probability of bubbles having a residence time more than 0.5 s by calculation	Calculated mean residence time/s	Effective C_L in the calculation	C_D in the calculation according to Eq. (10)
1	0.12	4.2	0.11	4.8	1.7	0.30–1.10
2	0.25	18.9	0.25	18.6	2.1	0.35–1.10
3	0.41	22.0	0.45	21.6	2.4	0.35–1.40
4	0.48	20.8	0.50	20.8	2.1	0.45–1.50
5	0.53	16.4	0.52	16.5	1.8	0.45–1.60

5. Conclusions

Bubble motion in a cavity is a common phenomenon in both nature and industrial processes. Previous studies typically focused on the motion of bubbles in stagnant water. In this work, due to the shearing of the liquid above the cavity and the turbulence within the cavity, single bubbles can be confined in the cavity sometimes for tens of seconds. The high liquid velocity and intense turbulence result in complex bubble motion. The increasing downward liquid velocity makes it easier for bubbles to be trapped and less likely to escape. With the increase of liquid flow rate, the coverage area of the bubble motion expands, and is closer to the center of the cavity. This shift increases the chances of the bubble being taken away from the cavity by the departing liquid. Thus, changes in flow rate alter the liquid flow field in the cavity, which in turn affects bubble trajectories, ultimately affecting both the mean residence time and the residence probability of bubbles.

Bubbles smaller than 2 mm in diameter are generally treated as rigid spheres in stagnant water. However, when such bubbles move in the cavity, they undergo severe deformation, complicating the modelling of bubble dynamics. From PIV data, not only the average liquid flow field can be obtained, but also the turbulent characteristics such as turbulent kinetic energy and turbulent time scale. Incorporating these turbulent characteristics into the liquid flow field allows for realistic estimation of the actual flow conditions experienced by the bubbles in the experiment. Based on the information of the liquid flow field, the forces acting on the bubble, including drag force, pressure gradient force and lift force, have been analyzed and evaluated. The drag coefficient is determined using the model of a contaminated system of Tomiyama *et al.*, and it has been confirmed that changing the value of C_D has no significant effect on the bubble motion. However, the deformability of the bubble has effect on the lift force. Our analysis conforms to the lift coefficient model of Adoua *et al.*, where C_L increases with bubble deformation. Experimental observations indicated that bubble aspect ratios changed continuously during motion, leading to variations in C_L. We use an effective lift coefficient to match the experimentally observed mean residence time and probability of bubbles having a residence time more than 0.5 s. By adjusting the effective lift coefficient, our model can approximately reproduce the experimental residence time and bubble position distributions in the cavity.

The behavior of bubbles in a complex flow field is studied experimentally, and the bubble trajectories and motion times matching the experiments are obtained through calculation, providing a new method for the study of bubble motion. However, our model assumes a quasi-two-dimensional cavity and liquid turbulence, which cannot fully represent bubble motion in a three-dimensional flow field. In the future, the thickness of the cavity in *z*-direction will be increased to explore the bubble motion under three-dimensional turbulence. In addition, this study does not quantify how specific factors influence the lift coefficient individually; and only the combined influencing effects of those specific factors are incorporated into the effective lift coefficient. When conducting subsequent research on the lift coefficient of bubbles in turbulence, different influencing factors, such as bubble deformation, turbulence and wall shear, can be quantified to develop a more generalized correlation for bubble lift coefficient.

CRediT Authorship Contribution Statement

Yuyun Bao: Writing – review & editing. **Xinyu Li:** Writing – original draft. **Ziqi Cai:** Resources. **Zhengming Gao:** Project administration. **J.J. Derksen:** Writing – review & editing.

Declaration of Competing interest

The authors declare no competing financial interest.

Acknowledgements

The authors gratefully acknowledge the financial support from the National Natural Science Foundation of China (22078008) and the China Petrochemical Corporation (Sinopec Group, project number: 222129). The authors are also grateful to Professor G. M. Evans (The University of Newcastle, Australia) for his valuable scientific support.

Supplementary Material

The assessment of the isotropic assumption can be found in the supplementary data.

Nomenclature

a	random number, –
$\boldsymbol{a}_{\mathrm{B}}$	acceleration of bubble, $\mathrm{m \cdot s^{-2}}$
C_{D}	drag force coefficient, –
C_{L}	lift force coefficient, –
C_{S}	Smagorinsky–Lilly constant, –
d_{B}	equivalent diameter of bubble, m
d_{c}	equivalent diameter of the channel, m
$\boldsymbol{e}_y$	unit vector, –
Eo	Eotvos number
$\boldsymbol{F}$	net force on bubble, N
$\boldsymbol{F}_{\mathrm{D}}$	drag force, N

$\boldsymbol{F}_{\mathrm{L}}$	lift force, N
$\boldsymbol{F}_{\mathrm{P}}$	pressure gradient force, N
$\boldsymbol{g}$	gravitational acceleration, m·s^{-2}
k	turbulent kinetic energy, m·s^{-2}
m_{a}	added mass of bubble, kg
m	mass of bubble, kg
M	Morton
N_{B}	bubble number, –
p	pressure, Pa
Re	Reynolds numbers of bubble
Re_{L}	Reynolds numbers of liquid flow in the channel
s_{ij}	resolved strain-rate tensor, s^{-1}
t_{res}	bubble residence time, s
$\bar{t}$	mean bubble residence time, s
t_{ts}	turbulence time scale, s
$\boldsymbol{u}_{\mathrm{B}}$	bubble velocity, m·s^{-1}
$\boldsymbol{u}_{\mathrm{L}}$	liquid velocity, m·s^{-1}
$\overline{\boldsymbol{u}_{\mathrm{L}}}$	average liquid velocity, m·s^{-1}
$\boldsymbol{u}_{\mathrm{L}}'$	fluctuating liquid velocity, m·s^{-1}
$\boldsymbol{u}_{\mathrm{L,rms}}$	liquid root-mean-square velocity, m·s^{-1}
$\boldsymbol{u}_{\mathrm{s}}$	slip velocity of bubble, m·s^{-1}
x	horizontal coordinate, m
y	vertical direction, m
z	depth direction, m
Δ	size of the interrogation window, m
Δt	time interval, s
ε	turbulent dissipation rate, m^{2}·s^{-3}
μ_{L}	viscosity of liquid, Pa·s

ν kinematic viscosity of liquid, $m^2 \cdot s^{-1}$

ρ_B density of bubble, $kg \cdot m^{-3}$

ρ_L density of liquid, $kg \cdot m^{-3}$

σ surface tension of air–liquid interface, $N \cdot m^{-1}$

$\boldsymbol{\tau}$ Reynolds stress, $N \cdot m^{-2}$

χ bubble aspect ratio, –

References

[1] K. Dewsbury, D. Karamanev, A. Margaritis, Hydrodynamic characteristics of free rise of light solid particles and gas bubbles in non-Newtonian liquids, *Chem. Eng. Sci.* 54 (21) (1999) 4825–4830.

[2] A. Ferreira, G. Pereira, J.A. Teixeira, F. Rocha, Statistical tool combined with image analysis to characterize hydrodynamics and mass transfer in a bubble column, *Chem. Eng. J.* 180 (2012) 216–228.

[3] S. Amirnia, J.R. de Bruyn, M.A. Bergougnou, A. Margaritis, Continuous rise velocity of air bubbles in non-Newtonian biopolymer solutions, *Chem. Eng. Sci.* 94 (2013) 60–68.

[4] H. Hessenkemper, T. Ziegenhein, D. Lucas, Contamination effects on the lift force of ellipsoidal air bubbles rising in saline water solutions, *Chem. Eng. J.* 386 (2020) 121589.

[5] J. Xu, M.R. Maxey, G.E. Karniadakis, Numerical simulation of turbulent drag reduction using micro-bubbles, *J. Fluid Mech.* 468 (2002) 271–281.

[6] W.C. Sanders, E.S. Winkel, D.R. Dowling, M. Perlin, S.L. Ceccio, Bubble friction drag reduction in a high-Reynolds-number flat-plate turbulent boundary layer, *J. Fluid Mech.* 552 (2006) 353–380.

[7] R.A. Verschoof, R.C.A. van der Veen, C. Sun, D. Lohse, Bubble drag reduction requires large bubbles, *Phys. Rev. Lett.* 117 (10) (2016) 104502.

[8] L.X. Zhou, R.X. Li, R.X. Du, Numerical simulation of the effect of void fraction and inlet velocity on two-phase turbulence in bubble–liquid flows, *Acta Mech. Sin.* 22 (5) (2006) 425–432.

[9] N.M. Aybers, A. Tapucu, The motion of gas bubbles rising through stagnant liquid, *Wärme Und Stoffübertragung* 2 (2) (1969) 118–128.

[10] A. Tomiyama, G.P. Celata, S. Hosokawa, S. Yoshida, Terminal velocity of single bubbles in surface tension force dominant regime, *Int. J. Multiph. Flow* 28 (9) (2002) 1497–1519.

[11] L. Liu, H.J. Yan, G.J. Zhao, Experimental studies on the shape and motion of air bubbles in viscous liquids, *Exp. Therm. Fluid Sci.* 62 (2015) 109–121.

[12] M.J. Pang, J.J. Wei, B. Yu, Numerical study of bubbly upflows in a vertical channel using the Euler–Lagrange two-way model, *Chem. Eng. Sci*. 65 (23) (2010) 6215–6228.

[13] G.L. Lane, M.P. Schwarz, G.M. Evans, Numerical modelling of gas–liquid flow in stirred tanks, *Chem. Eng. Sci*. 60 (8–9) (2005) 2203–2214.

[14] X.L. Li, G.H. Li, Modeling and simulation of hydrodynamic bubble–liquid turbulent flows in bubble-column reactors, *Chem. Eng. Technol*. 39 (12) (2016) 2380–2388.

[15] A.S.M.A. Islam, D.J. Bergstrom, Modelling bubble induced turbulence for gas–liquid bubbly flow in a vertical pipe, *Chem. Eng. Sci*. 197 (2019) 159–171.

[16] P. Lakshmanan, F. Peters, N. Fries, P. Ehrhard, Gas bubbles in simulation and experiment, *J. Colloid Interface Sci*. 354 (1) (2011) 364–372.

[17] T. Nate, D.M. Himmelblau, Mass transfer from large single bubbles at high Reynolds numbers, *AIChE J.* 13 (4) (1967) 697–702.

[18] J.M.T. Vasconcelos, S.P. Orvalho, S.S. Alves, Gas–liquid mass transfer to single bubbles: effect of surface contamination, *AIChE J*. 48 (6) (2002) 1145–1154.

[19] Y.Y. Bao, Z.C. Jiang, S.F. Tong, X.B. Huang, Z.Q. Cai, Z.M. Gao, Reactive mass transfer of single O_2 bubbles in a turbulent flow chamber, *Chem. Eng. Sci*. 207 (2019) 829–843.

[20] Y.Y. Bao, S.F. Tong, J.J. Zhang, Z.Q. Cai, Z.M. Gao, Reactive mass transfer of single bubbles in a turbulent flow chamber: discussion on the effects of slippage and turbulence, *Chem. Eng. Sci*. 231 (2021) 116253.

[21] Y.Y. Bao, R.T. Wang, S.G. Ma, K.J. Wen, Z.M. Gao, Z.Q. Cai, Reactive mass transfer of single bubbles in a turbulent flow chamber: the effect of temperature, *Chem. Eng. Sci*. 274 (2023) 118679.

[22] K.V. Sharp, R.J. Adrian, PIV study of small-scale flow structure around a Rushton turbine, *AIChE J*. 47 (4) (2001) 766–778.

[23] S. Baldi, M. Yianneskis, On the quantification of energy dissipation in the impeller stream of a stirred vessel from fluctuating velocity gradient measurements, *Chem. Eng. Sci*. 59 (13) (2004) 2659–2671.

[24] J. Sheng, H. Meng, R.O. Fox, A large eddy PIV method for turbulence dissipation rate estimation, *Chem. Eng. Sci.* 55 (20) (2000) 4423–4434.

[25] J. Smagorinsky, General circulation experiments with the primitive equations: I. the basic experiment, *Mon. Wea. Rev.* 91 (3) (1963) 99–164.

[26] C. Meneveau, T.S. Lund, The dynamic Smagorinsky model and scale-dependent coefficients in the viscous range of turbulence, *Phys. Fluids* 9 (12) (1997) 3932–3934.

[27] G. Bertens, D. van der Voort, H. Bocanegra-Evans, W. van de Water, Large-eddy estimate of the turbulent dissipation rate using PIV, *Exp. Fluids* 56 (5) (2015) 89.

[28] W.J. Liang, D.F. Wang, Z.Q. Cai, Z.P. Li, X.B. Huang, Z.M. Gao, J.J. Derksen, A.E. Komrakova, Deformation and breakup of single drop in laminar and transitional jet flows, *Chem. Eng. J.* 386 (2020) 121812.

[29] R. Weber, F. Boysan, W.H. Ayers, J. Swithenbank, Simulation of dispersion of heavy particles in confined turbulent flows, *AIChE J.* 30 (3) (1984) 490–492.

[30] G.K. Batchelor, An Introduction to Fluid Dynamics, Cambridge University Press, Cambridge, (1967).

[31] A. Tomiyama, I. Kataoka, I. Zun, T. Sakaguchi, Drag coefficients of single bubbles under normal and micro gravity conditions, *JSME Int. J., Ser. B* 41 (2) (1998) 472–479.

[32] A. Tomiyama, H. Tamai, I. Zun, S. Hosokawa, Transverse migration of single bubbles in simple shear flows, *Chem. Eng. Sci.* 57 (11) (2002) 1849–1858.

[33] I. Ẑun, The transverse migration of bubbles influenced by walls in vertical bubbly flow, *Int. J. Multiph. Flow* 6 (6) (1980) 583–588.

[34] T.R. Auton, The lift force on a spherical body in a rotational flow, *J. Fluid Mech.* 183 (1987) 199–218.

[35] D. Legendre, J. Magnaudet, The lift force on a spherical bubble in a viscous linear shear flow, *J. Fluid Mech.* 368 (1998) 81–126.

[36] A.A. Kulkarni, Lift force on bubbles in a bubble column reactor: experimental analysis, *Chem. Eng. Sci.* 63 (6) (2008) 1710–1723.

[37] Y. Takagi, N. Fujisawa, T. Nakano, A. Nashimoto, Cylinder wake influence on the tonal noise

and aerodynamic characteristics of a NACA0018 airfoil, *J. Sound Vib.* 297 (3–5) (2006) 563–577.

[38] C. Zhang, X.G. Yuan, Y.Q. Luo, G.Y.T. Yu, Prediction of species concentration distribution using a rigorous turbulent mass diffusivity model for bubble column reactor simulation part II: analogy between turbulent mass and momentum transfer in toluene emissions biodegradation process, *Chem. Eng. Sci.* 189 (2018) 360–368.

[39] A. Chouippe, E. Climent, D. Legendre, C. Gabillet, Numerical simulation of bubble dispersion in turbulent Taylor–Couette flow, *Phys. Fluids* 26 (4) (2014) 043304.

[40] M.A. Pakhomov, V.I. Terekhov, Modeling of turbulent structure of an upward polydisperse gas–liquid flow, *Fluid Dyn.* 50 (2) (2015) 229–239.

[41] S.S. Long, X.G. Yang, J. Yang, M. Sommerfeld, C.Y. Xue, Large eddy simulation of bubble column bubbly flow considering subgrid-scale turbulent diffusion effects and bubble oscillation, *Chem. Eng. Technol.* 46 (9) (2023) 1791–1799.

[42] X.S. Zhang, J.H. Wang, D.C. Wan, Euler–Lagrange study of bubble breakup and coalescence in a turbulent boundary layer for bubble drag reduction, *Phys. Fluids* 33 (3) (2021) 037105.

[43] R. Adoua, D. Legendre, J. Magnaudet, Reversal of the lift force on an oblate bubble in a weakly viscous linear shear flow, *J. Fluid Mech.* 628 (2009) 23–41.

[44] P.M. Doran, Bioprocess Engineering Principles, Academic press, London, (1995).

[45] I.K. Kure, H.A. Jakobsen, J. Solsvik, Experimental study of interfacial mass transfer from single CO_2 bubbles ascending in stagnant water, *Chem. Eng. Sci.* 287 (2024) 119684.

[46] H. Hessenkemper, T. Ziegenhein, R. Rzehak, D. Lucas, A. Tomiyama, Lift force coefficient of ellipsoidal single bubbles in water, *Int. J. Multiph. Flow* 138 (2021) 103587.

[47] M.K. Zand, S. Puttinger, M. Saeedipour, A new approach to unravel the lift force phenomenon of a single bubble rising in stagnant and sheared liquids, *Int. J. Multiph. Flow* 188 (2025) 105219.

[48] T. Ziegenhein, A. Tomiyama, D. Lucas, A new measuring concept to determine the lift force for distorted bubbles in low Morton number system: results for air/water, *Int. J. Multiph. Flow* 108 (2018) 11–24.

[49] S.L. Shu, N. El Bahraoui, F. Bertrand, J. Chaouki, A bubble-induced turbulence model for gas–liquid bubbly flows in airlift columns, pipes and bubble columns, *Chem. Eng. Sci.* 227 (2020) 115945.

[50] D. Kim, J. Kim, Improved modeling of wall effects on interfacial momentum exchange for wall-bounded bubbly flows based on resolved simulations, *Chem*. *Eng*. *Sci*. 250 (2022) 117332.

[51] J.Y. Feng, I.A. Bolotnov, Effect of the wall presence on the bubble interfacial forces in a shear flow field, *Int*. *J. Multiph. Flow* 99 (2018) 73–85.